

# Superfluid stiffness of magic-angle twisted bilayer graphene

<https://doi.org/10.1038/s41586-024-08494-7>

Received: 17 June 2024

Accepted: 5 December 2024

Published online: 5 February 2025

 Check for updates

Miuko Tanaka<sup>1,2,9</sup>, Joel I.-j. Wang<sup>1,9</sup>✉, Thao H. Dinh<sup>3</sup>, Daniel Rodan-Legrain<sup>1</sup>, Sameia Zaman<sup>1,4</sup>, Max Hays<sup>1</sup>, Aziza Almanakly<sup>1,4</sup>, Bharath Kannan<sup>1,4,8</sup>, David K. Kim<sup>5</sup>, Bethany M. Niedzielski<sup>5</sup>, Kyle Serniak<sup>1,6</sup>, Mollie E. Schwartz<sup>6</sup>, Kenji Watanabe<sup>6</sup>, Takashi Taniguchi<sup>7</sup>, Terry P. Orlando<sup>1,4</sup>, Simon Gustavsson<sup>1,8</sup>, Jeffrey A. Grover<sup>1</sup>, Pablo Jarillo-Herrero<sup>3</sup>✉ & William D. Oliver<sup>1,3,4</sup>✉

The physics of superconductivity in magic-angle twisted bilayer graphene (MATBG) is a topic of keen interest in moiré systems research, and it may provide an insight into the pairing mechanism of other strongly correlated materials such as high-critical-temperature superconductors. Here we use d.c. transport and microwave circuit quantum electrodynamics to directly measure the superfluid stiffness of superconducting MATBG through its kinetic inductance. We find the superfluid stiffness to be much larger than expected from conventional Fermi liquid theory. Rather, it is comparable to theoretical predictions<sup>1</sup> and recent experimental indications<sup>2</sup> of quantum geometric effects that are dominant at the magic angle. The temperature dependence of the superfluid stiffness follows a power law, which contraindicates an isotropic Bardeen–Cooper–Schrieffer (BCS) model. Instead, the extracted power-law exponents indicate an anisotropic superconducting gap, whether interpreted in the Fermi liquid framework or by considering the quantum geometry of flat-band superconductivity. Moreover, a quadratic dependence of the superfluid stiffness on both d.c. and microwave current is observed, which is consistent with the Ginzburg–Landau theory. Taken together, our findings show that MATBG is an unconventional superconductor with an anisotropic gap and strongly suggest a connection between quantum geometry, superfluid stiffness and unconventional superconductivity in MATBG. The combined d.c.–microwave measurement platform used here is applicable to the investigation of other atomically thin superconductors.

Stacking two graphene sheets with a finite twist angle between individual crystallographic axes forms a moiré superlattice. In the special case known as MATBG, a twist angle of approximately 1.05° results in flat energy bands, which facilitate strong electron–electron interactions. Multiple phases of matter have been observed in MATBG, including correlated insulators, superconductors, strange metal phases and topological insulating states, all accessible through an applied gate voltage that controls the carrier density<sup>3–7</sup>. Of particular interest is its superconducting state, as it shares a notable resemblance to other interaction-driven superconductors, including cuprates and heavy-fermion superconductors<sup>4,6–9</sup>. Observing superconductivity in the flat-band regime suggests that the superfluid stiffness is determined by the energy-band dispersion as well as its geometry in phase space<sup>1,10–15</sup>. Investigating superconductivity in MATBG could, therefore, provide a fundamental insight into the mechanisms that underlie unconventional superconductivity in this and other materials.

However, so far, there have been relatively few experimental investigations of the unconventional pairing in superconducting moiré systems. Many of the conventional approaches used to study the gap structure of bulk superconductors, such as the magnetic penetration depth, Meissner effect, thermal transport and inelastic neutron scattering, are difficult to apply to van der Waals heterostructures. This is, in part, due to the small size of typical two-dimensional samples—atomically thin with a few-micrometre-square area and an inhomogeneous twist angle—and their generally ultralow carrier density<sup>16</sup>.

The electromagnetic properties of a superconductor are described by the constitutive relation (in the London gauge) as

$$\mathbf{j} = -D_s \mathbf{A}, \quad (1)$$

where  $D_s$  is the superfluid stiffness,  $\mathbf{j}$  is the two-dimensional current density (current per unit width) and  $\mathbf{A}$  is the vector potential<sup>17</sup>. The

<sup>1</sup>Research Laboratory of Electronics, Massachusetts Institute of Technology, Cambridge, MA, USA. <sup>2</sup>Institute for Solid State Physics, The University of Tokyo, Kashiwa, Japan. <sup>3</sup>Department of Physics, Massachusetts Institute of Technology, Cambridge, MA, USA. <sup>4</sup>Department of Electrical Engineering and Computer Science, Massachusetts Institute of Technology, Cambridge, MA, USA. <sup>5</sup>Lincoln Laboratory, Massachusetts Institute of Technology, Lexington, MA, USA. <sup>6</sup>Research Center for Electronic and Optical Materials, National Institute for Materials Science, Tsukuba, Japan. <sup>7</sup>Research Center for Materials Nanoarchitectonics, National Institute for Materials Science, Tsukuba, Japan. <sup>8</sup>Present address: Atlantic Quantum, Cambridge, MA, USA. <sup>9</sup>These authors contributed equally: Miuko Tanaka, Joel I.-j. Wang. <sup>✉</sup>e-mail: joelwang@mit.edu; pjariello@mit.edu; william.oliver@mit.edu

# Article

inverse of the superfluid density is the kinetic inductance  $L_K = 1/D_s$ . Therefore, one can directly access  $D_s$  by measuring  $L_K$  in an a.c. circuit. In Fermi liquid theory,  $D_s$  is directly proportional to the Cooper pair density  $n_s$  and inversely proportional to the charge carrier effective mass  $m_{\text{eff}}$ :

$$D_s = \frac{2n_s e^2}{m_{\text{eff}}}. \quad (2)$$

Moreover, the temperature dependence of  $n_s$  is characteristic of the pairing symmetry and gap structure of a superconductor due to its quasiparticle spectrum at a finite temperature. Characterizing the kinetic inductance has proven to be a promising method for studying the nature of superconductivity in unconventional bulk superconductors<sup>18,19</sup> and homogeneous thin films<sup>20–22</sup>.

In this work, we directly measure the superfluid stiffness of MATBG through the kinetic inductance  $L_K$  and its dependence on temperature, d.c. bias current and microwave power. The measured superfluid stiffness is much larger than conventional values estimated from the band dispersion in a Fermi liquid framework. Rather, the magnitude of the measured  $D_s$  value is consistent with theoretical works incorporating quantum geometric contributions that are predicted to dominate at the magic angle<sup>1</sup>. Furthermore, the temperature dependence of the superfluid stiffness exhibits a power-law behaviour that contradicts an isotropic BCS model. This behaviour aligns with the expectations for unconventional superconductivity in MATBG and is consistent with theoretical predictions for an anisotropic, flat-band superconductor in which the quantum metric is taken into account<sup>23</sup>. Taken together, our results indicate both an anisotropic gap and a quantum geometric contribution to the unconventional superconductivity in MATBG.

## Device configuration

We use a superconducting quarter-wavelength ( $\lambda/4$ ) waveguide resonator to characterize the kinetic inductance of MATBG (Fig. 1). A  $\lambda/4$  resonator terminated directly to ground has a resonance frequency of  $f = \frac{1}{2\pi\sqrt{L_{\text{eff}}C_{\text{eff}}}}$ , where  $L_{\text{eff}}$  and  $C_{\text{eff}}$  are the effective inductance and capacitance of the resonator, respectively.

By contrast, when the resonator is terminated to ground through a superconducting MATBG sample, the resonance frequency shifts to a new frequency  $f = \frac{1}{2\pi\sqrt{\tilde{L}_{\text{eff}}(V_{\text{BG}})C_{\text{eff}}}}$ , due to the appreciable kinetic inductance of the MATBG that is added to the resonator intrinsic inductance, where  $\tilde{L}_{\text{eff}}$  includes the additional gate-dependent effective inductance of the MATBG-terminated resonator. As described below, the added inductance of the MATBG sample can be extracted from shifts in the resonance frequency (Fig. 1a).

Figure 1b shows the aluminium (Al) superconducting circuit used in this experiment. A common throughline couples capacitively to both control and experiment resonators to measure their resonance frequencies. The experiment resonator is terminated with a hexagonal boron nitride (hBN)-MATBG-hBN heterostructure (Fig. 1c) positioned on an Al back gate, to which a voltage is applied to tune the MATBG carrier density. Moreover, five galvanic contacts—superconducting at cryogenic temperatures—connect the MATBG to the microwave resonator, the ground plane and three d.c. probe electrodes (Fig. 1c). This design enables us to perform both microwave and d.c. transport characterization of the MATBG device.

## Measuring the kinetic inductance

Figure 2 shows the d.c. and microwave characterization of a representative MATBG device as a function of back-gate voltage  $V_{\text{BG}}$  (Methods provides details about the measurement setup). The differential resistance  $dV/dI_{\text{d.c.}}$  of the MATBG sample is first measured

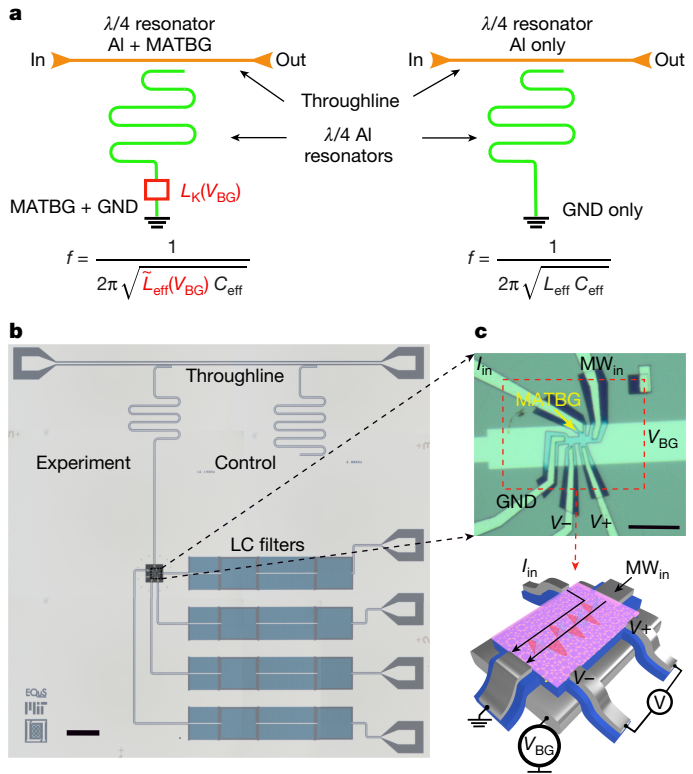


**Fig. 1 | Kinetic inductance measurement and device configuration.**

**a**, Schematic of the MATBG inductance measurement circuit. The Al quarter-wave ( $\lambda/4$ ) ‘experiment resonator’ terminates to ground through the MATBG sample. The Al quarter-wave ( $\lambda/4$ ) ‘control resonator’ terminates directly to ground with Al. Both resonators couple capacitively to the throughline, which is probed by a vector network analyser (not shown) to measure the resonance frequencies of the experiment and control resonators. The resonance frequency of the experiment resonator is used to infer the gate-voltage-dependent inductance of the MATBG. For comparison, the control resonator is used to check the inductance characterization technique using an Al termination, a well-characterized BCS material (Methods). **b**, Optical image of a  $5 \times 5 \text{ mm}^2$  chip comprising the resonators, throughline, d.c. bias lines, filters and the ground plane, patterned from 250-nm-thick Al on a high-resistivity Si substrate. The d.c. electrodes are LC filtered on chip to reduce bias noise. Scale bar, 400  $\mu\text{m}$ . **c**, Zoomed-in image and schematic of the MATBG sample on the experiment resonator. The hBN–MATBG–hBN heterostructure is placed on an Al back gate to voltage bias the MATBG and change its carrier density. Scale bar, 10  $\mu\text{m}$ .

with a standard four-probe lock-in technique at zero d.c. bias current (Fig. 2). As expected, the device is resistive at the charge neutrality point (CNP) at filling factor  $v = 0$  and in the insulating regions around  $v = \pm 2$  and  $v = 3$ . The d.c. resistance vanishes after passing the  $v = \pm 2$  insulating regions, indicating the presence of superconductivity in both hole-doped ( $v < 0$ ) and electron-doped ( $v > 0$ ) regimes (Fig. 2a). We further parameterize the superconducting region by sweeping the d.c. bias current  $I_{\text{d.c.}}$  and back-gate voltage  $V_{\text{BG}}$  in both the hole-doped (Fig. 2c) and electron-doped (Fig. 2d) regimes.

We use a vector network analyser connected to the throughline to measure the microwave transmission coefficient  $S_{21}$  as a function of frequency, from which the resonance frequency of the resonator is extracted<sup>24</sup>. Figure 2b plots the magnitude  $|S_{21}|$  as a function of frequency and back-gate voltage  $V_{\text{BG}}$ . There are two notable features in the data: (1) a constant resonant frequency  $f_r \approx 3.8 \text{ GHz}$  at the CNP ( $v = 0$ ) and in the insulating regions ( $v = \pm 2$ ); and (2) a back-gate-dependent resonance frequency in the superconducting regions, just beyond the insulating regions ( $v \lesssim -2$  and  $v \gtrsim 2$ ). The resonance frequency is generally gate dependent in the superconducting regions defined using the d.c. transport measurements (Fig. 2c,d).

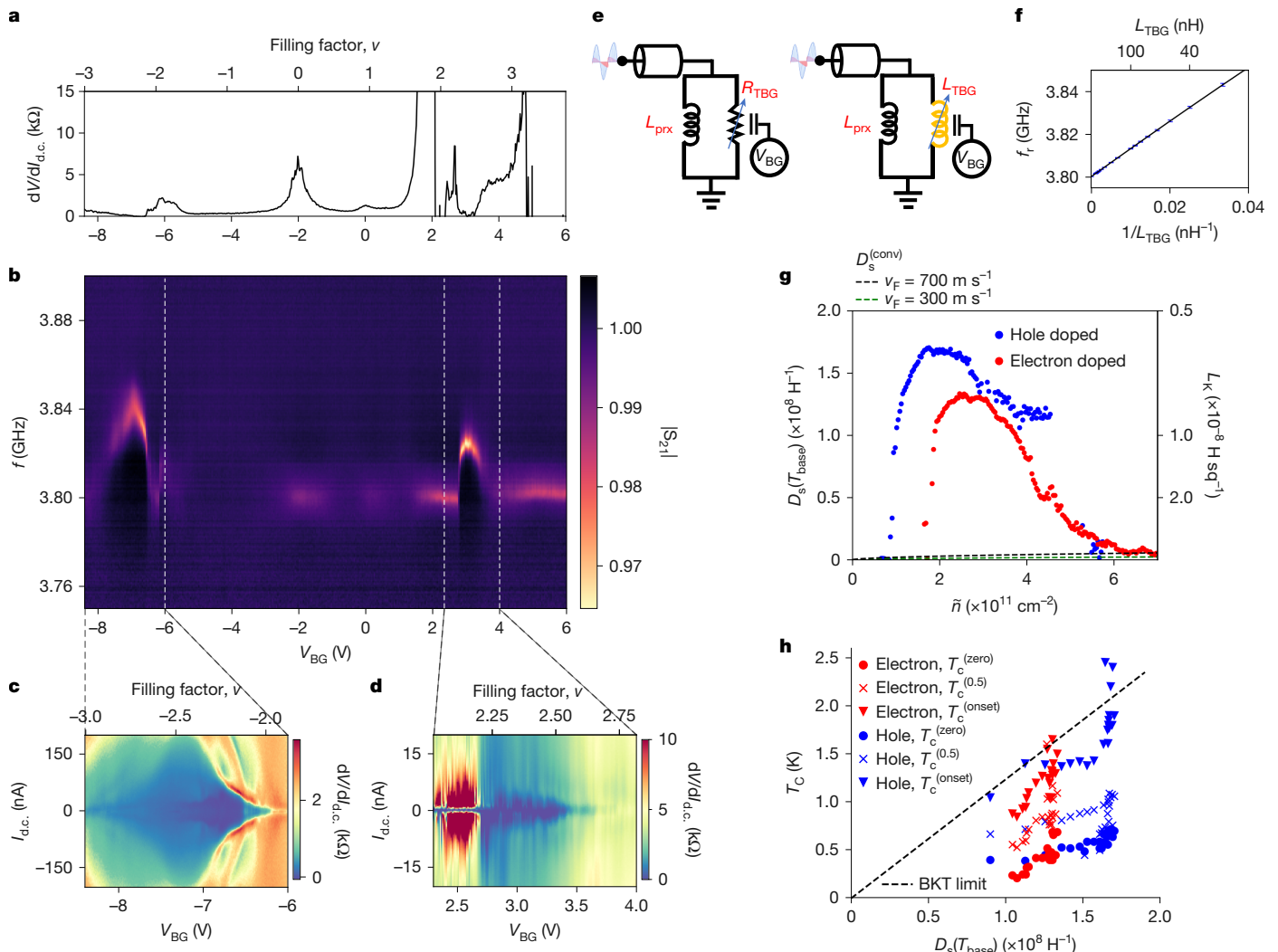


**Fig. 2 | Gate-voltage-dependent d.c. and microwave characteristics.**

**a**, Differential resistance  $dV/dI_{d.c.}$  of the MATBG termination at zero bias current as a function of the back-gate voltage  $V_{BG}$ . The top axis represents the filling factor  $v$ . **b**, Microwave transmission coefficient  $|S_{21}|$  versus  $V_{BG}$ . The resonant frequency (bright line) shifts in the zero-resistance region in **a**, near filling factors  $v = \pm 2$ . The resonance remains essentially constant in the high-resistance region. **c,d**, Differential resistance  $dV/dI_{d.c.}$  as a function of  $V_{BG}$  and  $I_{d.c.}$  for hole-doped (**c**) and electron-doped (**d**) MATBG. The top axis represents the filling factor  $v$ . **e**, Lumped-element model for the MATBG termination of the resonator and the electrode-induced proximity effect when voltage biased in the highly resistive regime (left) and the superconducting regime (right).

See the main text for a description of the circuit elements. **f**, Simulated resonance frequency  $f_r$  versus inverse of the MATBG kinetic inductance  $1/L_{TBG}$ . The top axis represents  $L_{TBG}$ . **g**, Superfluid stiffness  $D_s$  at base temperature  $T_{base}$  as a function of effective carrier density  $\tilde{n}$ , measured with respect to  $|v| = 2$ . The error bars are too small to discern, with errors ranging from  $1 \times 10^6$  to  $5 \times 10^6 \text{ H}^{-1}$ . The black and green dashed curves are the conventional contribution to the superfluid stiffness from Fermi liquid theory:  $D_s^{(\text{conv})} = e^2 \tilde{n} v_F / \hbar k_F$  assuming  $v = 700 \text{ m s}^{-1}$  and  $v = 300 \text{ m s}^{-1}$ , respectively. **h**, Critical temperature  $T_c$  and the corresponding superfluid stiffness  $D_s$  at base temperature  $T_{base}$  as tuned by  $V_{BG}$ . The black dashed line represents the BKT upper limit  $T_c = \pi \hbar^2 D_s(T_{base}) / 8e^2 k_B$ .

These behaviours can be modelled by a lumped-element model involving a gate-tunable kinetic inductance  $L_{TBG}$  of the superconducting MATBG, a finite MATBG resistance  $R_{TBG}$  and a parallel, constant inductance  $L_{\text{prox}}$  originating from the Al-proximity-matized MATBG edge (Fig. 2e). Using this lumped-element model in conjunction with microwave simulations, we extract the kinetic inductance of the MATBG termination given a measured resonance frequency of the resonator (Methods). Figure 2f plots  $f_r$  as a function of  $1/L_{TBG}$ . The frequency shift  $\Delta f_r = f_r - f_0$  depends almost linearly on  $1/L_{TBG}$ .

## Superfluid stiffness and quantum geometry

The kinetic inductance of MATBG enables us to directly measure the superfluid stiffness and its trends with physical parameters. Assuming the active MATBG region has the same aspect ratio as the device itself,

given by length  $l$  and width  $w$ , the total measured superfluid stiffness  $D_s = l/(wL_{TBG})$  at the base temperature  $T_{base}$  is plotted versus the effective carrier density in Fig. 2g for hole-doped (blue) and electron-doped (red) MATBG.

In two-dimensional superconductors exhibiting a Berezinskii–Kosterlitz–Thouless (BKT) transition,  $D_s$  and  $T_c$  are related by the expression  $\frac{\pi \hbar^2 D_s(0)}{8e^2} \geq k_B T_c$  (refs. 25,26). As illustrated in Fig. 2h, the measured superfluid stiffness  $D_s(T_{base})$  and critical temperature  $T_c$  determined by d.c. resistance measurements exhibit a relationship that is generally consistent with this formula, providing additional confidence in our experimental measurement of  $D_s$  (Methods describes the determination of critical temperatures).

We compare the measured  $D_s$  values with existing theoretical models. The conventional superfluid stiffness  $D_s^{(\text{conv})}$  predicted in the Fermi liquid framework yields  $D_s^{(\text{conv})} = e^2 \tilde{n} v_F / \hbar k_F$ , where  $\tilde{n}$  is the

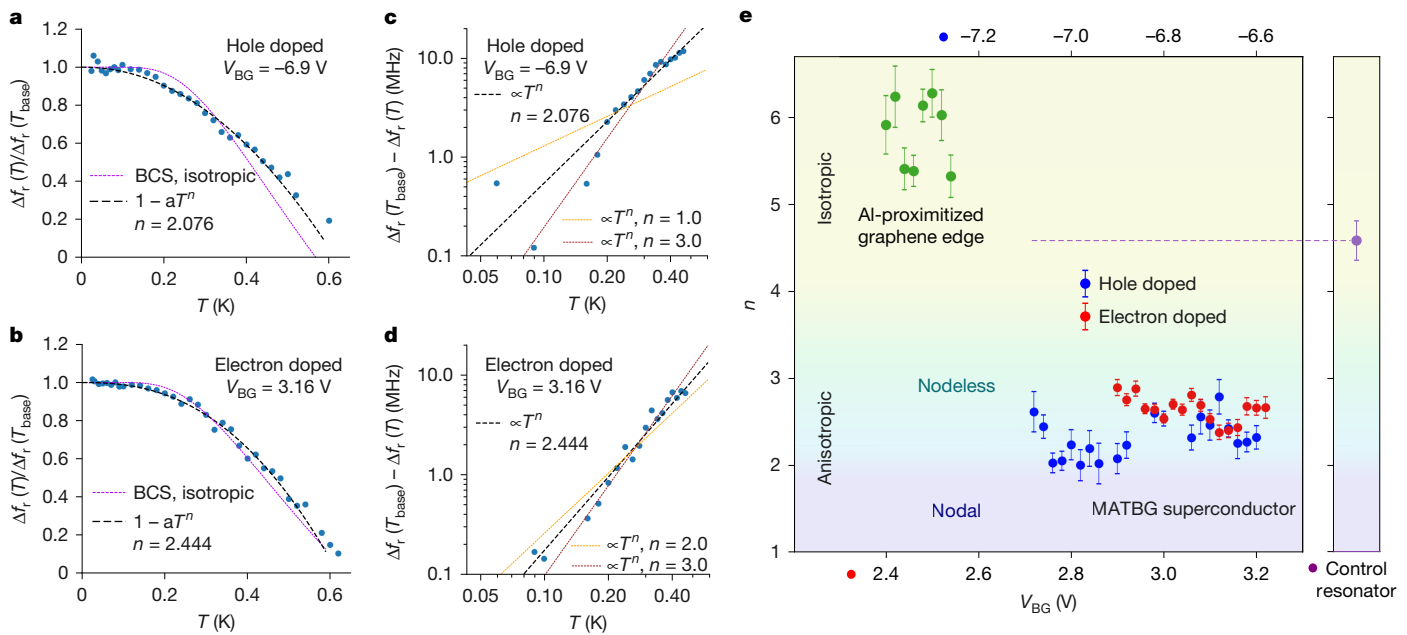


**Fig. 3 | Temperature-dependent shift in resonant frequency due to varying superfluid stiffness.** **a,b**, Temperature dependence of  $\Delta f_r(T)/\Delta f_r(T_{\text{base}})$  for  $T < T_{\text{BKT}}$  (Supplementary Information shows the determination of  $T_{\text{BKT}}$ ) in the hole-doped (**a**) and electron-doped (**b**) regimes. The blue dots represent the experimental data, the black dashed lines depict the power-law fitting and the purple dashed lines depict the exponential function in the BCS isotropic model. **c,d**, Log–log plot of  $\Delta f_r(T_{\text{base}}) - \Delta f_r(T)$  in the hole-doped (**c**) and electron-doped (**d**) regimes. The orange and brown dashed lines depict the power law with

exponents of  $n = 1.0$  and  $3.0$  and  $n = 2.0$  and  $3.0$ , respectively. **e**, Power-law fit exponent of the temperature dependence of the resonance in the hole-doped superconducting region (blue dots), electron-doped superconducting region (red dots), insulating region in which the Al-proximity graphene terminate the resonator (green dots) and the control resonator (purple dot in the right panel). Error bars represent the standard deviation derived from the power-law fitting process.

effective carrier density measured relative to  $|v| = 2$ ,  $k_F = \sqrt{2\pi/\tilde{n}}$  is the Fermi wavevector and  $v_F$  is the Fermi velocity. From the  $dV/dI_{\text{d.c.}}$  versus  $I_{\text{d.c.}}$  measurements<sup>2,27</sup>, we estimate  $v_F$  to be in the range of approximately 300–700 m s<sup>-1</sup> (Methods). The measured  $D_s$  value is an order-of-magnitude greater than the conventional contribution  $D_s^{(\text{conv})}$ .

This discrepancy indicates that mechanisms beyond Fermi liquid theory need to be considered to fully describe the superconductivity in MATBG. In a flat-band system like MATBG, in which the Fermi velocity becomes exceedingly small, it is proposed that superfluidity and supercurrent can arise if the system exhibits non-trivial quantum geometry<sup>10</sup>.

This geometry is manifest as overlapping Wannier functions between neighbouring lattice sites, influenced by higher-energy bands<sup>11,12</sup>, creating an extended state that enables the transport of interacting particles. At the magic angle, the conventional contribution of the superfluid stiffness  $D_s^{(\text{conv})}$  in MATBG is suppressed, and the overall superfluid stiffness  $D_s$  is predominantly set by the quantum geometric contribution  $D_s^{(\text{QG})}$ .

Our measurements indicate the maximum superfluid stiffness of  $1.7 \times 10^8$  H<sup>-1</sup> for hole-doped MATBG and  $1.25 \times 10^8$  H<sup>-1</sup> for electron-doped MATBG (Fig. 2g). Both are comparable with the theoretical prediction of approximately  $0.7$ – $5.2 \times 10^8$  H<sup>-1</sup> for  $D_s^{(\text{QG})}$  (refs. 11,12), suggesting that the dominant contribution to superfluid stiffness may arise from quantum geometry<sup>1,2,10–13,28,29</sup>.

We also note that the superfluid stiffness directly measured in this experiment is consistent with the value inferred from measurements of the critical current density, as reported recently<sup>2</sup>.

anisotropy in unconventional superconductors<sup>18,19</sup>. At low temperatures ( $T < 0.3T_c$ ), the conventional superfluid stiffness  $D_s^{(\text{conv})}$  in superconductors with isotropic gaps exhibits an exponential temperature dependence  $\delta D_s^{(\text{conv})}(T)/D_s^{(\text{conv})}(0) \propto \sqrt{\frac{2\pi\Delta_0}{k_B T}} \exp\left(-\frac{\Delta_0}{k_B T}\right)$ , where  $\delta D_s^{(\text{conv})}(T) = D_s^{(\text{conv})}(0) - D_s^{(\text{conv})}(T)$  is the change in stiffness with temperature  $T$ , and  $\Delta_0$  is the superconducting gap at zero temperature<sup>17,18</sup>. By contrast, superconductors with an anisotropic gap or nodes exhibit a power-law temperature dependence  $\delta D_s^{(\text{conv})}(T)/D_s^{(\text{conv})}(0) \propto T^n$  (ref. 18). In two-dimensional momentum space, nodal gaps exhibit an exponent  $n = 1$  (linear dependence) in the clean limit and  $n = 2$  in the dirty limit, whereas nodeless anisotropic gaps display  $n > 2$  (ref. 30). The isotropic  $s$ -wave gap with an exponential dependence typically displays  $n > 4$  in this formalism<sup>31,32</sup>. By contrast, recent theoretical studies suggest that the quantum geometric contribution  $D_s^{(\text{QG})}$  follows a power-law temperature dependence, with the value of the exponent also depending on the structure of the superconducting gap<sup>23</sup>.

To test these ideas, we study the temperature dependence of the MATBG kinetic inductance. Figure 3a,b show  $\Delta f_r(T)/\Delta f_r(T_{\text{base}})$ , which is equivalent to  $D_s(T)/D_s(T_{\text{base}})$  for temperatures  $T < T_{\text{BKT}}$ , where  $T_{\text{BKT}}$  is the BKT temperature (Supplementary Information shows the determination of  $T_{\text{BKT}}$ ) in the hole-doped ( $V_{\text{BG}} = -6.9$  V) and electron-doped ( $V_{\text{BG}} = 3.16$  V) regimes.

The trends clearly deviate from the exponential dependence expected for a BCS isotropic model, indicating unconventional superconductivity in MATBG. Furthermore, they fit well to a power-law function with exponent  $n = 2.08$  and  $n = 2.44$ , respectively, which is also confirmed in the logarithmic plot of  $\Delta f_r(T_{\text{base}}) - \Delta f_r(T) \propto \delta D_s(T)$  (Fig. 3c,d). We extract the power-law exponent across the entire superconducting dome in both electron- and hole-doped regimes, with  $n$  ranging from 2 to 3 (Fig. 3e). This suggests an anisotropic superconducting gap in the Fermi liquid framework  $D_s^{(\text{conv})}$  (refs. 18,19). By contrast, when the same measurement and analysis is performed in the insulating MATBG regime, in which the  $\lambda/4$  resonator is terminated only by

## Temperature dependence

The temperature dependence of the superfluid stiffness and the associated quasiparticle spectrum have been widely used to probe the gap

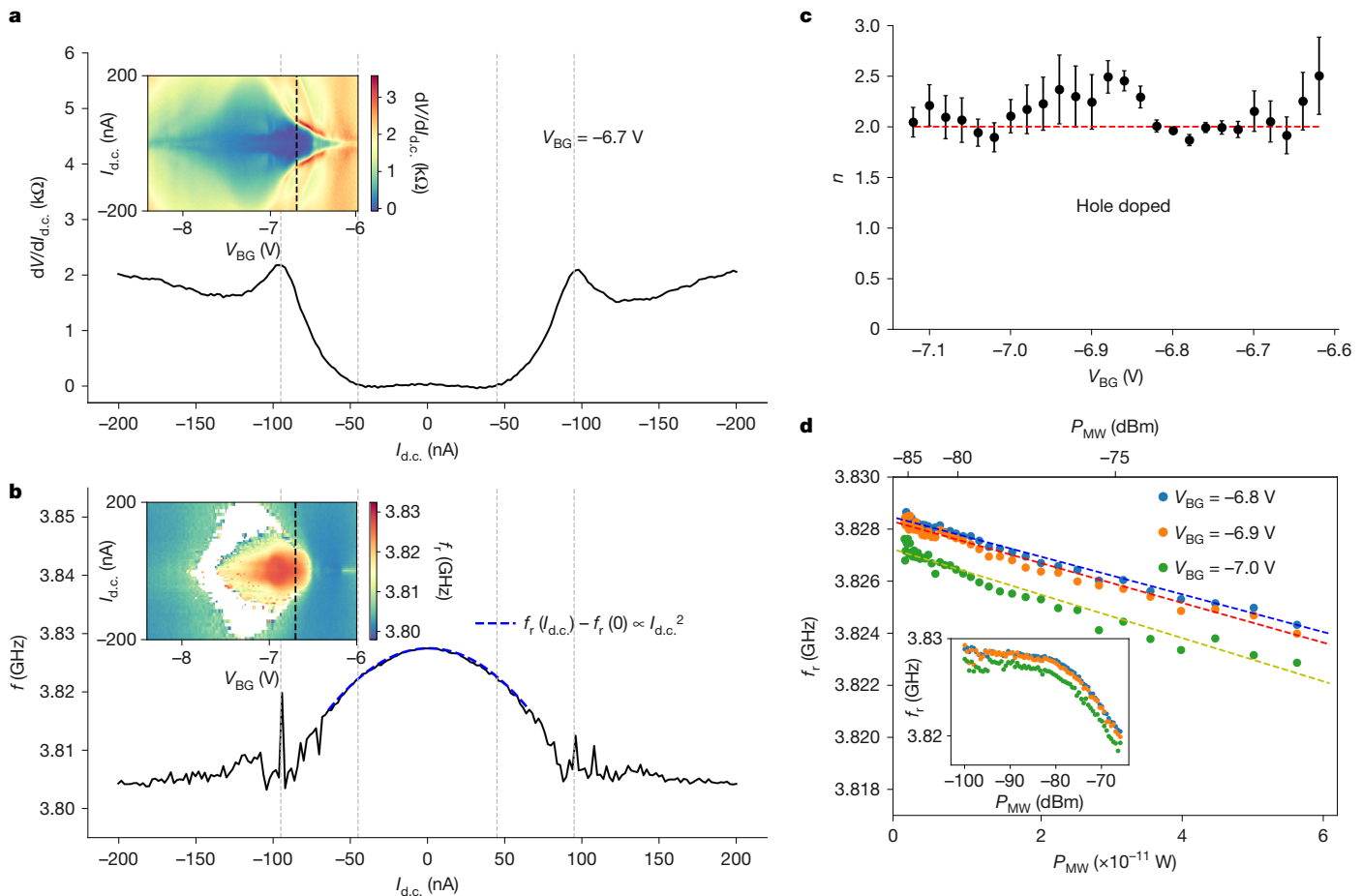


**Fig. 4 | d.c. bias and microwave power dependence of resonant frequency.** **a**, Differential resistance  $dV/dI_{\text{d.c.}}$  dependence on bias current  $I_{\text{d.c.}}$  for back-gate voltage  $V_{\text{BG}} = -6.7 \text{ V}$  (black dashed line in the inset). Inset: two-dimensional colour map versus  $V_{\text{BG}}$  and  $I_{\text{d.c.}}$ . **b**, Resonant frequency  $f_r$  dependence on  $I_{\text{d.c.}}$  for back-gate voltage  $V_{\text{BG}} = -6.7 \text{ V}$  (black dashed line in the inset). Inset: two-dimensional colour map of  $dV/dI_{\text{d.c.}}$  versus  $V_{\text{BG}}$  and  $I_{\text{d.c.}}$ . The blue dashed

curve indicates a quadratic fit to the data. **c**, Exponents  $n$  of the power-law fitting  $f_r(I_{\text{d.c.}} = 0) - f_r(I_{\text{d.c.}}) \propto I_{\text{d.c.}}^n$  as a function of  $V_{\text{BG}}$ . Error bars represent the standard deviation derived from the fitting process. The red dashed line indicates  $n = 2$ . **d**, Microwave power  $P_{\text{MW}}$  dependence of  $f_r$  at  $V_{\text{BG}} = -6.8, -6.9$  and  $-7.0 \text{ V}$ . The blue dashed lines indicate a linear dependence with power, corresponding to a quadratic dependence on the microwave current amplitude.

the Al-proximitized graphene edge, or on the Al control resonator, we observe higher exponents ( $n \geq 4.6$ ), a characteristic of isotropic  $s$ -wave superconductivity.

Notably, this power-law behaviour with  $n$  ranging from 2 to 3 also aligns with theoretical predictions for  $D_s^{(\text{QG})}$  in a superconductor with an anisotropic gap<sup>23</sup>. Finally, we note that other extrinsic disorders may also lead to anisotropic or even nodal gap<sup>33,34</sup>, or, conversely, lift the unprotected gap nodes<sup>35,36</sup>. Data from an additional sample showing similar results are discussed in the Methods.

## Bias current and power dependence

We now explore the dependence of superfluid stiffness on the d.c. bias current. We apply a d.c. bias current  $I_{\text{d.c.}}$  through terminal  $I_+$  (Fig. 1c). Figure 4a,b displays the d.c. differential resistance  $dV/dI_{\text{d.c.}}$  and the resonant frequency  $f_r$  versus current  $I_{\text{d.c.}}$  at  $V_{\text{BG}} = -6.7 \text{ V}$ , respectively. Importantly,  $f_r$  shows a noticeable dependence in the range of currents  $0 \leq I_{\text{d.c.}} \leq 40 \text{ nA}$ , even around zero bias, whereas the d.c. resistance consistently remains a constant ( $0 \Omega$ ). The fact that only the resonance frequency changes with  $I_{\text{d.c.}}$  as the sample remains superconducting indicates that it is the superfluid stiffness that changes ( $D_s$  is suppressed and  $L_K$  increases) with increasing  $I_{\text{d.c.}}$ . At any given gate voltage in the superconducting domes, the frequency shift exhibits a quadratic dependence (concave down) on the d.c. bias current (Fig. 4b,c).

Moreover, the resonant frequency  $f_r$  decreases linearly with the microwave power  $P_{\text{MW}}$  applied to the feedline (Fig. 4d). Considering that  $P_{\text{MW}}$  is proportional to the square of the a.c. current amplitude ( $P_{\text{MW}} \propto I_{\text{MW}}^2$ ), this similarly indicates that the reduction in  $f_r$  depends quadratically on the microwave current.

The quadratic current dependence is described by the Ginzburg–Landau theory and by BCS theory when considering pair breaking by the finite momentum of Cooper pairs. It is expressed as  $D_s(I)/D_s(0) = 1 - (I/I^*)^2$  or  $L_K(I) \propto L_0[1 + (I/I^*)^2]$ , where  $I^*$  is on the order of the depairing current<sup>37–40</sup>, and is commonly observed in thin-film superconductors<sup>41–47</sup>. To our knowledge, the d.c. bias current dependence of superfluid stiffness arising from the quantum geometry contribution to the superfluid stiffness,  $D_s^{(\text{QG})}$ , has not yet been discussed theoretically.

Our devices do not exhibit the nonlinear Meissner effect, which refers to a linear bias current dependence of the superfluid stiffness. Instead, the quadratic dependence on current holds up to  $I_c$  throughout the superconducting dome<sup>48,49</sup> (Supplementary Information).

## Discussion and conclusion

We develop and demonstrate a measurement platform comprising a microwave resonator terminated by an atomically thin sample of interest—in this work, MATBG—that is contacted to enable both d.c. and microwave measurements. The resonator with MATBG termination

features a quality factor exceeding 1,000 at 20 mK (Supplementary Information), capable of discerning changes in the superfluid stiffness at the 1% level. We use this platform to measure the MATBG kinetic inductance—a direct measurement of the superfluid stiffness—as a function of parameters that lead to pair breaking, including thermal excitation, bias current and microwave drive power.

The directly measured MATBG superfluid stiffness is an order-of-magnitude larger than the conventional contribution predicted by band dispersion in a Fermi liquid framework. Instead, this value aligns well with a theoretical model that incorporates quantum geometry, in which a  $D_s$  value of this magnitude for MATBG is expected<sup>1,10–13,23,28,29</sup>. This result, along with recent d.c. transport measurements<sup>2</sup>, underscores the potentially substantial role of quantum geometry in understanding the unconventional superconductivity of MATBG.

The temperature dependence of the MATBG superfluid stiffness follows a power-law dependence in both hole-doped and electron-doped regimes. This behaviour deviates from the exponential dependence observed in superconductors with isotropic s-wave pairing as well as the linear dependence observed in clean nodal superconductors. Our data generally fall in the range of power-law exponents  $n = 2\text{--}3$ .

In the conventional Fermi liquid framework, the measured exponents indicate the presence of an anisotropic gap in MATBG<sup>18,19</sup>. The exponents together with the quadratic bias current dependence of  $D_s$ —which point to the absence of a nonlinear Meissner effect in our measurements—indicate a nodeless anisotropic gap in MATBG. We do not rule out the possibility that our results may reflect an intrinsically nodal gap that is lifted due to the presence of disorder, for example, from twist-angle variations.

However, the contribution of quantum geometry to the low-energy quasiparticle spectrum remains an open question. Therefore, it is not guaranteed that the conventional analysis based on power-law exponents would apply precisely. In a quantum geometry framework, recent theoretical calculations<sup>23</sup> for anisotropic gaps that include a quantum geometric contribution predict an exponent of 3, which is consistent with our measured exponents.

In summary, we develop and demonstrate a platform that directly measures the superfluid stiffness of atomically thin superconducting systems. Our experimental measurements of the superfluid stiffness in MATBG reveal phenomena that apparently go beyond the conventional Fermi liquid theory and strongly suggest a connection to multiband quantum geometry in a flat-band superconductor. Although it is beyond the scope of this experiment to distinguish the relative contributions of the Fermi liquid and quantum geometry frameworks to the superfluid stiffness, our results indicate anisotropic pairing in MATBG in both frameworks. These findings lay the groundwork for future theoretical studies to deepen our understanding of flat-band superconductivity. During the preparation of our manuscript, we became aware of a complementary work<sup>50</sup>.

## Online content

Any methods, additional references, Nature Portfolio reporting summaries, source data, extended data, supplementary information, acknowledgements, peer review information; details of author contributions and competing interests; and statements of data and code availability are available at <https://doi.org/10.1038/s41586-024-08494-7>.

- Törmä, P., Peotta, S. & Bernevig, B. A. Superconductivity, superfluidity and quantum geometry in twisted multilayer systems. *Nat. Rev. Phys.* **4**, 528–542 (2022).
- Tian, H. et al. Evidence for Dirac flat band superconductivity enabled by quantum geometry. *Nature* **614**, 440–444 (2023).
- Cao, Y. et al. Correlated insulator behavior at half-filling in magic-angle graphene superlattices. *Nature* **556**, 80–84 (2018).
- Cao, Y. et al. Unconventional superconductivity in magic-angle graphene superlattices. *Nature* **556**, 43–50 (2018).
- Cao, Y. et al. Strange metal in magic-angle graphene with near Planckian dissipation. *Phys. Rev. Lett.* **124**, 076801 (2020).
- Balents, L., Dean, C. R., Efetov, D. K. & Young, A. F. Superconductivity and strong correlations in moiré flat bands. *Nat. Phys.* **16**, 725–733 (2020).
- Andrei, E. Y. & MacDonald, A. H. Graphene bilayers with a twist. *Nat. Mater.* **19**, 1265–1275 (2020).
- Oh, M. et al. Evidence for unconventional superconductivity in twisted bilayer graphene. *Nature* **600**, 240–245 (2021).
- Cao, Y. et al. Nematicity and competing orders in superconducting magic-angle graphene. *Science* **372**, 264–271 (2021).
- Peotta, S. & Törmä, P. Superfluidity in topologically nontrivial flat bands. *Nat. Commun.* **6**, 8944 (2015).
- Hu, X., Hyart, T., Pikulin, D. I. & Rossi, E. Geometric and conventional contribution to the superfluid weight in twisted bilayer graphene. *Phys. Rev. Lett.* **123**, 237002 (2019).
- Julkka, A., Peltonen, T. J., Liang, L., Heikkilä, T. T. & Törmä, P. Superfluid weight and Berezinskii-Kosterlitz-Thouless transition temperature of twisted bilayer graphene. *Phys. Rev. B* **101**, 060505 (2020).
- Xie, F., Song, Z., Lian, B. & Bernevig, B. A. Topology-bounded superfluid weight in twisted bilayer graphene. *Phys. Rev. Lett.* **124**, 167002 (2020).
- Hofmann, J. S., Chowdhury, D., Kivelson, S. A. & Berg, E. Heuristic bounds on superconductivity and how to exceed them. *npj Quantum Mater.* **7**, 83 (2022).
- Ma, C. et al. Moiré band topology in twisted bilayer graphene. *Nano Lett.* **20**, 6076–6083 (2020).
- Andrei, E. Y. et al. The marvels of moiré materials. *Nat. Rev. Mater.* **6**, 201–206 (2021).
- Tinkham, M. *Introduction to Superconductivity: Second Edition* (Dover Publications, 2004).
- Prozorov, R. & Giannetta, R. W. Magnetic penetration depth in unconventional superconductors. *Supercond. Sci. Technol.* **19**, R41 (2006).
- Hardy, W., Kamal, S. & Bonn, D. *Magnetic Penetration Depths in Cuprates: A Short Review of Measurement Techniques and Results* (Springer, 2002).
- Böttcher, C. et al. Circuit quantum electrodynamics detection of induced two-fold anisotropic pairing in a hybrid superconductor–ferromagnet bilayer. *Nat. Phys.* **20**, 1609–1615 (2024).
- Phan, D. et al. Detecting induced  $p\pm ip$  pairing at the Al-InAs interface with a quantum microwave circuit. *Phys. Rev. Lett.* **128**, 107701 (2022).
- Weitzel, A. et al. Sharpness of the Berezinskii-Kosterlitz-Thouless transition in disordered NbN films. *Phys. Rev. Lett.* **131**, 186002 (2023).
- Penttilä, R. P. S., Huhtinen, K.-E. & Törmä, P. Flat-band ratio and quantum metric in the superconductivity of modified Lieb lattices. Preprint at <https://arxiv.org/abs/2404.12993> (2024).
- Probst, S., Song, F. B., Bushev, P. A., Ustinov, A. V. & Weides, M. Efficient and robust analysis of complex scattering data under noise in microwave resonators. *Rev. Sci. Instrum.* **86**, 024706 (2015).
- Emery, V. & Kivelson, S. Importance of phase fluctuations in superconductors with small superfluid density. *Nature* **374**, 434–437 (1995).
- Kosterlitz, J. M. & Thouless, D. J. in *Basic Notions Of Condensed Matter Physics* 493–515 (CRC Press, 1973).
- Berdyyugin, A. I. et al. Out-of-equilibrium criticalities in graphene superlattices. *Science* **375**, 430–433 (2022).
- Wu, F. Topological chiral superconductivity with spontaneous vortices and supercurrent in twisted bilayer graphene. *Phys. Rev. B* **99**, 195114 (2019).
- Törmä, P. Essay: where can quantum geometry lead us? *Phys. Rev. Lett.* **131**, 240001 (2023).
- Hirschfeld, P. J. & Goldenfeld, N. Effect of strong scattering on the low-temperature penetration depth of a d-wave superconductor. *Phys. Rev. B* **48**, 4219 (1993).
- Ropponi, M. et al. Bulk evidence of anisotropic s-wave pairing with no sign change in the kagome superconductor  $\text{CsV}_3\text{Sb}_5$ . *Nat. Commun.* **14**, 667 (2023).
- Teknowijoyo, S. et al. Nodeless superconductivity in the type-II Dirac semimetal  $\text{PdTe}_2$ : London penetration depth and pairing-symmetry analysis. *Phys. Rev. B* **98**, 024508 (2018).
- Khvalyuk, A. V., Charpentier, T., Roch, N., Sacépé, B. & Feigel'Man, M. V. Near power-law temperature dependence of the superfluid stiffness in strongly disordered superconductors. *Phys. Rev. B* **109**, 144501 (2024).
- Ghosal, A., Randeria, M. & Trivedi, N. Inhomogeneous pairing in highly disordered s-wave superconductors. *Phys. Rev. B* **65**, 014501 (2001).
- Mishra, V. et al. Lifting of nodes by disorder in extended-s-state superconductors: application to ferropnictides. *Phys. Rev. B* **79**, 094512 (2009).
- Cho, K. et al. Energy gap evolution across the superconductivity dome in single crystals of  $(\text{Ba}_{1-x}\text{K}_x)\text{Fe}_2\text{As}_2$ . *Sci. Adv.* **2**, e1600807 (2016).
- Gittelman, J., Rosenblum, B., Seidel, T. & Wicklund, A. Nonlinear reactance of superconducting films. *Phys. Rev.* **137**, A527 (1965).
- Enpuku, K., Hoashi, M., Doi, H. D. H. & Kisu, T. K. T. Modulation of kinetic inductance of high  $T_c$  superconducting thin films with bias current. *Jpn. J. Appl. Phys.* **32**, 3804 (1993).
- Kubo, T. Superfluid flow in disordered superconductors with Dynes pair-breaking scattering: depairing current, kinetic inductance, and superheating field. *Phys. Rev. Res.* **2**, 033203 (2020).
- Anthore, A., Pothier, H. & Esteve, D. Density of states in a superconductor carrying a supercurrent. *Phys. Rev. Lett.* **90**, 127001 (2003).
- Luomaahaara, J., Vesterinen, V., Grönberg, L. & Hassel, J. Kinetic inductance magnetometer. *Nat. Commun.* **5**, 4872 (2014).
- Ku, J., Manucharyan, V. & Bezryadin, A. Superconducting nanowires as nonlinear inductive elements for qubits. *Phys. Rev. B* **82**, 134518 (2010).
- Claassen, J., Adrian, S. & Soulen, R. Large non-linear kinetic inductance in superconductor/normal metal bilayer films. *IEEE Trans. Appl. Supercond.* **9**, 4189–4192 (1999).

44. Thomas, C. N., Withington, S., Sun, Z., Skyrme, T. & Goldie, D. J. Nonlinear effects in superconducting thin film microwave resonators. *New J. Phys.* **22**, 073028 (2020).
45. Vissers, M. R. et al. Frequency-tunable superconducting resonators via nonlinear kinetic inductance. *Appl. Phys. Lett.* **107**, 062601 (2015).
46. Kirsh, N. et al. Linear and nonlinear properties of a compact high-kinetic-inductance WSi multimode resonator. *Phys. Rev. A* **16**, 044017 (2021).
47. Zhao, S., Withington, S., Goldie, D. J. & Thomas, C. N. Nonlinear properties of supercurrent-carrying single-and multi-layer thin-film superconductors. *J. Low Temp. Phys.* **199**, 34–44 (2020).
48. Carrington, A., Giannetta, R., Kim, J. & Giapintzakis, J. Absence of nonlinear Meissner effect in  $\text{YBa}_2\text{Cu}_3\text{O}_{6.95}$ . *Phys. Rev. B* **59**, R14173 (1999).
49. Li, M.-R., Hirschfeld, P. & Wölfle, P. Is the nonlinear Meissner effect unobservable? *Phys. Rev. Lett.* **81**, 5640 (1998).
50. Banerjee, A. et al. Superfluid stiffness of twisted trilayer graphene superconductors. *Nature* <https://doi.org/10.1038/s41586-024-08444-3> (2025).

**Publisher's note** Springer Nature remains neutral with regard to jurisdictional claims in published maps and institutional affiliations.

Springer Nature or its licensor (e.g. a society or other partner) holds exclusive rights to this article under a publishing agreement with the author(s) or other rightsholder(s); author self-archiving of the accepted manuscript version of this article is solely governed by the terms of such publishing agreement and applicable law.

© The Author(s), under exclusive licence to Springer Nature Limited 2025

# Article

## Methods

### Device fabrication

We begin with a 250 nm Al film deposited on high-resistivity Si wafers. The circuit elements, including a transmission line, resonators, LC filters and d.c. probe lines (Fig. 1a,b), are patterned using photolithography and an Al wet-etch process. A Ti/Al (5/30 nm) back gate is defined using electron-beam lithography and electron-beam evaporation in the cut-out window used to host the van der Waals heterostructures. Details of the Al fabrication process can be found in ref. 51.

The incorporation of van der Waals heterostructures onto the patterned chips uses standard mechanical exfoliation and dry-polymer-based techniques<sup>52,53</sup>. The hBN flake exfoliated on the SiO<sub>2</sub> substrate is transferred onto a Ti/Al (5/30 nm) back gate. After removing the polymer by soaking in chloroform, the top surface of the hBN is cleaned by contact-mode atomic force microscopy scanning. After an iterative stacking procedure, a stack of hBN and MATBG is released onto the bottom hBN.

After transferring the heterostructures, the hBN–MATBG–hBN stack is patterned into a Hall-bar geometry using electron-beam lithography and reactive ion etching. Superconducting contacts are made to the MATBG edge using reactive ion etching followed by the thermal evaporation of Ti/Al. The superconducting bridging between the contacts, the Al resonator and the ground plane is made using electron-beam lithography and *in situ* ion milling followed by Al deposition.

### Measurement setup

The experiment is performed in a Bluefors XLD-1000 dilution refrigerator with a base temperature of approximately 20 mK. Attenuation at several cryogenic stages is used to reduce the number of thermal photons at higher-temperature stages from reaching the device. We use a -20 dB directional coupler to pump a Josephson travelling-wave parametric amplifier (TWPA) mounted at the base temperature to pre-amplify the resonator probe tone. To reduce the impact of reflections of the TWPA pump on the device, we add a circulator between the device and TWPA. After the TWPA, there are additional isolators, filters and a high-electron mobility transistor amplifier thermally anchored to the 3 K stage. At room temperature (300 K), we further amplify (MITEQ) the output signal. Each d.c. line connected to the device is lowpass filtered with a  $\pi$ -filter at 3 K, and a QFilter (Quantum Machines) at the mixing chamber stage. Extended Data Fig. 1 shows the schematic of the measurement setup.

### Microwave simulations

The presence and absence of resonator gate dependence are modelled by the lumped-element circuits<sup>54</sup> (Fig. 2e), representing the coplanar waveguide terminated by MATBG under the two following conditions. When the MATBG is highly resistive, that is, at the CNP or in insulating regions, the MATBG termination is modelled as a resistor ( $R_{\text{TBG}} \gg 1 \text{ k}\Omega$ ) in parallel with an inductive element  $L_{\text{prx}}$  (Fig. 2e, left). The inductance  $L_{\text{prx}}$  represents the edge of graphene that is in close proximity to the Ti/Al electrodes, from which the edge inherits a superconducting order parameter. The inductance  $L_{\text{prx}}$  of the proximitized graphene edge is essentially independent of gate voltage  $V_{\text{BG}}$  due to the robust doping that results from the proximity effect, leading to a fixed resonance frequency<sup>52,55</sup>. By contrast, when the MATBG enters the superconducting phase, the resistance  $R_{\text{TBG}}$  vanishes and is replaced by a kinetic inductance  $L_{\text{TBG}}$  that arises from the superfluid condensate, resulting in a second parallel inductor that terminates the coplanar waveguide and is  $V_{\text{BG}}$  dependent (Fig. 2e, right). The resonance frequency  $f_r$  varies with gate voltage  $V_{\text{BG}}$  in the superconducting region determined by d.c. measurements (Fig. 2c,d), reaching maximum values at around  $V_{\text{BG}} = -6.8 \text{ V}$  and  $V_{\text{BG}} = 3 \text{ V}$  in the hole-doped and electron-doped regimes, respectively. Outside the

insulating and superconducting regions, the MATBG bulk behaves like a normal metal with a small, non-zero resistance, which strongly damps the resonator and prevents an accurate extraction of its resonance frequency<sup>24,54</sup>.

We test the validity of this model with two additional experiments. First, we fabricate a Bernal (AB)-stacked bilayer graphene device that nominally has the same geometry and metallization as the MATBG device. The Bernal device exhibits resonance at around 4 GHz when biased near the CNP to be highly insulating (Extended Data Fig. 2b). As the Bernal-stacked bilayer graphene is non-superconducting at this bias point, this observation indicates that the observed resonance at around 4 GHz is not unique to the MATBG sample as well as unrelated to its intrinsic superconductivity.

Second, we verify this model by applying a perpendicular magnetic field to the Bernal (AB)-stacked bilayer graphene device. Extended Data Fig. 2b shows the magnetic field dependence of the resonance in the bilayer graphene device that is gate biased at the CNP. The resonance at 4.24 GHz vanishes at around 0.42 mT, which is much smaller than the critical magnetic field of either the resonator Al film ( $H_c \approx 10 \text{ mT}$ ) or the superconducting MATBG, but consistent with a weak superconducting link to ground formed by proximitized graphene<sup>56</sup>. These tests verify the role of the proximitized graphene in maintaining a  $\lambda/4$  resonator with a resonance frequency that only shifts about 1% between insulating and superconducting MATBG regimes.

To analyse the model, we use the SONNET finite-element solver to determine the relationship between the resonant frequency shift and the kinetic inductance. We model the Al film as a two-dimensional perfect electrical conductor on a 350  $\mu\text{m}$  silicon (Si) substrate, with 500  $\mu\text{m}$  of vacuum above the film, and calculate the S parameters at the microwave ports.

We set the resistance  $R_{\text{TBG}} = 100 \text{ k}\Omega$  to represent the insulating regime and sweep  $L_{\text{prx}}$  to reproduce the observed base frequency of 3.8 GHz (Extended Data Fig. 2d, inset). This yields  $L_{\text{prx}} = 1.32 \text{ nH}$ , consistent with a previous study of the Josephson inductance in proximitized graphene<sup>55</sup>. Using this value, we calculate the  $L_{\text{TBG}}$  dependence of  $f_r$  (Extended Data Fig. 2d). The frequency shift  $\Delta f_r = f_r - 3.8 \text{ GHz}$  depends almost linearly on  $1/L_{\text{TBG}} \propto D_s$ .

Throughout this simulation, the capacitance between the MATBG and back gate is fixed at 3 fF, a value estimated based on the dimension and dielectric properties of the bottom hBN. We find that the resonance frequency is insensitive to this capacitance (Extended Data Fig. 2c). Also, we check the  $L_{\text{TBG}}$  dependence of  $f_r$  with several different values of  $L_{\text{prx}}$  (Extended Data Fig. 2d,e). The linear dependence between  $\Delta f_r$  and  $1/L_{\text{TBG}}$  holds for different values of  $L_{\text{prx}}$ , which justifies the analysis assuming  $\Delta f_r \propto D_s$ .

To illustrate the impact of possible normal regions caused by contact resistance, disorder and twist-angle inhomogeneity in the MATBG device, we perform simulations incorporating a finite resistance in parallel and series configurations. As shown in Extended Data Fig. 2f,g, the presence of normal regions affects the quality factor but does not result in any discernable frequency shift, thereby not impacting the measurement of  $L_{\text{TBG}}$  (Extended Data Fig. 2f,g).

### Al control resonator and resonance in the insulating phase of MATBG

We characterize the Al control resonator in the absence of MATBG to test our protocol for measuring the superfluid stiffness and to confirm that the MATBG-terminated resonator temperature and power dependence are dominated by the MATBG.

Extended Data Fig. 3b plots the resonance frequency of the  $\lambda/4$  Al control resonator terminated directly to ground (that is, without MATBG). As the resonant frequency is  $f_r = \frac{1}{2\pi\sqrt{(L_C + L_K)\epsilon}}$  (where  $L_C \gg L_K$  is the geometric inductance), the relation  $f_r(T_{\text{base}})/f_r(T) - 1$  is proportional to  $L_K$ . The behaviour is well fit by the conventional isotropic

BCS Fermi liquid model, consistent with the conventional superconductivity present in Al (Extended Data Fig. 3c). The power-law fit gives an exponent of 4.585, consistent with previous reports for Al and isotropic gaps in general<sup>31,32</sup>. The shift in resonance frequency due to the kinetic inductance in the Al-only control resonator is much smaller than the MATBG-terminated Al experiment resonator, in part because Al (250 nm) is much thicker than MATBG (approximately 1 nm). This means that geometric inductance dominates in the Al-only resonator. The microwave power dependence of  $f_r$  is negligible compared with that in the experimental MATBG resonator (Extended Data Fig. 3d).

Extended Data Fig. 4b,c presents the temperature dependence of the resonance for the MATBG-terminated resonator measured at a back-gate voltage of  $V_{BG} = 2.44$  V in the insulating region near  $\nu = 2$ . Here the MATBG termination itself is shunted by its Al-proximitized edge. In this case, the temperature dependence of the resonance remains constant below 0.5 K, in contrast to MATBG biased in the superconducting phase, and we fit it using an isotropic BCS model with  $T_c = 1.2$  K. Here also, the power-law exponent  $n = 5.405$  is consistent with an isotropic gap for the proximitized region<sup>31,32</sup>. We used this resonance frequency as a standard reference when analysing the frequency shift due to the MATBG kinetic inductance:  $\Delta f(V_{BG}, T) = f_r(V_{BG}, T) - f_r(V_{BG} = 2.44 \text{ V}, T)$ .

The microwave power dependence of  $f_r$  is negligible in the insulating regime compared with that in the superconducting regime (Extended Data Fig. 4d). This indicates that the power dependence presented in the main text for the MATBG-terminated resonator is primarily due to the MATBG superconductivity.

### Estimation of Fermi velocity

In systems with a low inelastic scattering rate, the velocity of electron flow can reach the Fermi velocity, leading to non-equilibrium carrier generation known as the Schwinger mechanism. As MATBG has a Dirac cone with a much lower Fermi velocity than monolayer graphene, this effect occurs at relatively small currents, resulting in a critical-current-like behaviour in the normal state<sup>2,27,57</sup>.

Here the critical current in the normal state  $I_{cn}$  is related to the Fermi velocity using the expression  $v_n = \frac{J_{cn}}{\tilde{n}e}$ , where  $J_{cn}$  is the critical current density and  $\tilde{n}$  is the effective carrier density measured relative to  $|\nu| = 2$ . Experimentally determining  $I_{cn}$  provides an estimate for the Fermi velocity. In a previous study under a finite magnetic field, which was used to suppress superconductivity, it was reported that  $I_{cn}$  features a ‘bell-like’ shape in the vicinity of  $\nu = 2$ . The superconducting critical current  $I_c$  is coincident with  $I_{cn}$  in the underdoped regime, and they split in the overdoped regime<sup>2</sup>. We observe a similar behaviour in the peak of  $dV/dI_{dc}$  (Extended Data Fig. 5a) and estimate the Fermi velocity from the larger  $dV/dI_{dc}$  peak (Extended Data Fig. 5c). The conventional contribution to superfluid density (Fig. 3) is calculated based on this Fermi velocity.

### Determination of critical temperature

The critical temperature values presented in Fig. 2h are determined as follows (Extended Data Fig. 6a).

1. Linear fits are performed for the normal region and the region in which the resistance drops (Extended Data Fig. 6, grey dashed lines), referred to as line 1 and line 2.
2.  $T_c^{(onset)}$  is determined by the intersection of line 1 and line 2.
3.  $T_c^{(0.5)}$  is determined by the point at which line 2 crosses half the value of the intercept of line 1.
4.  $T_c^{(zero)}$  is determined by the point at which line 2 crosses zero resistance.

$T_c^{(0.5)}$  is approximately 1 K across most of the gate-tunable area (Extended Data Fig. 6b,c) and consistent with previous reports on MATBG<sup>4</sup>.

### Additional sample

In another device with essentially the same design and fabrication process, we observed qualitatively similar results, although it exhibited more spatial inhomogeneity, which results in multiple  $T_c$  and  $I_c$  values. Extended Data Fig. 7 shows the d.c. and microwave response of this second device as a function of  $V_{BG}$ . The behaviour qualitatively matches the first device with the following notable differences.

1. The electron-doped superconducting region does not exhibit complete zero resistance, whereas the first device shows zero resistance.
2. The hole-doped superconducting region shows multiple critical currents, which is thought to be due to the spatial inhomogeneity of the twist angle.
3. The base frequency is 4.2 GHz at the gate voltage at which the MATBG is highly insulating, indicating  $L_{prx}$  is approximately 0.9 nH.

Extended Data Fig. 8 presents the magnitude of the superfluid stiffness, which—like the first device—is much larger than the conventional Fermi liquid theory would predict (Extended Data Fig. 8c). The relation between  $T_c$  and  $D_s$  is again consistent with the BKT theory (Extended Data Fig. 8d).

Extended Data Fig. 9 shows the temperature dependence in the hole-doped SC region. Although the temperature dependence of  $f_r$  and  $D_s$  have multiple steps due to having multiple regions with different  $T_c$  values (Extended Data Fig. 9a,b), the low-temperature power-law analysis is still a valid means to extract results in the low-excitation limit. Extended Data Fig. 9c presents the power-law exponent  $n$  obtained using the fitting at  $T < 0.3T_c$ . The exponent is  $n \approx 1.3\text{--}3.2$ , which is comparable with the first device in indicating an anisotropic pairing.

The d.c. bias dependence below the smallest  $I_c$  value showed a quadratic behaviour and is also consistent with the first device (Extended Data Fig. 10).

### Data availability

The data that support the findings of this study are available from the corresponding authors upon reasonable request and with the cognizance of our US government sponsors who funded the work.

51. Yan, F. et al. The flux qubit revisited to enhance coherence and reproducibility. *Nat. Commun.* **7**, 12964 (2016).
52. Wang, J. I.-J. et al. Coherent control of a hybrid superconducting circuit made with graphene-based van der Waals heterostructures. *Nat. Nanotechnol.* **14**, 120–125 (2019).
53. Wang, L. et al. One-dimensional electrical contact to a two-dimensional material. *Science* **342**, 614–617 (2013).
54. Pozar, D. M. *Microwave Engineering* (John Wiley & Sons, 2011).
55. Schmidt, F. E., Jenkins, M. D., Watanabe, K., Taniguchi, T. & Steele, G. A. A ballistic graphene superconducting microwave circuit. *Nat. Commun.* **9**, 4069 (2018).
56. Bretheau, L. et al. Tunnelling spectroscopy of Andreev states in graphene. *Nat. Phys.* **13**, 756–760 (2017).
57. Schwinger, J. On gauge invariance and vacuum polarization. *Phys. Rev.* **82**, 664 (1951).

**Acknowledgements** We acknowledge helpful discussions with P. Törmä, L. Levitov, S. Todadri, M. Ropponi, K. Ishihara, T. Kitamura and Y. Yanase. We thank L. Ateshian, D. Rower, P. Harrington and the device packaging team at the MIT Lincoln Laboratory for technical assistance. This research was funded in part by the US Army Research Office grant no. W911NF-22-1-0023, by the National Science Foundation QIIT-QAQS grant no. OMA-1936263, by the Air Force Office of Scientific Research grant no. FA2386-21-1-4058 and by the Under Secretary of Defense for Research and Engineering under Air Force contract no. FA8702-15-D-0001. M.T. acknowledges support from the JSPS KAKENHI (grant no. 23K19026), Murata Science and Education Foundation, and JST PRESTO (grant no. JPMJPR24H7). P.J.-H. acknowledges support by the National Science Foundation (DMR-1809802), the Gordon and Betty Moore Foundation’s EPiQS Initiative through grant no. GBMF9463, the Fundacion Ramon Areces and the CIFAR Quantum Materials program. D.R.-L. acknowledges support from the Rafael del Pino Foundation. K.W. and T.T. acknowledge support from the JSPS KAKENHI (grant nos. 21H05233 and 23H02052) and World Premier International Research Center Initiative (WPI), MEXT, Japan. Any opinions, findings, conclusions or recommendations expressed in this material are those of the author(s) and do not necessarily reflect the views of the Under Secretary of Defense for Research and Engineering or the US Government.

# Article

**Author contributions** J.-j.W. conceived and designed the experiment. M.T., J.-j.W., T.H.D. and M.H. performed the microwave simulation. M.T., J.-j.W., T.H.D., S.Z., D.R.-L., D.K.K., B.M.N., K.S. and M.E.S. contributed to the device fabrication. M.T., J.-j.W., T.H.D., S.Z., D.R.-L., A.A. and B.K. participated in the measurements. M.T., J.-j.W. and M.H. analysed the data. K.W. and T.T. grew the hBN crystal. J.-j.W., M.T. and W.D.O. led the paper writing, and all other authors contributed to the text. J.A.G., T.P.O., S.G., P.J.-H., J.-j.W. and W.D.O. supervised the project.

**Competing interests** The authors declare no competing interests.

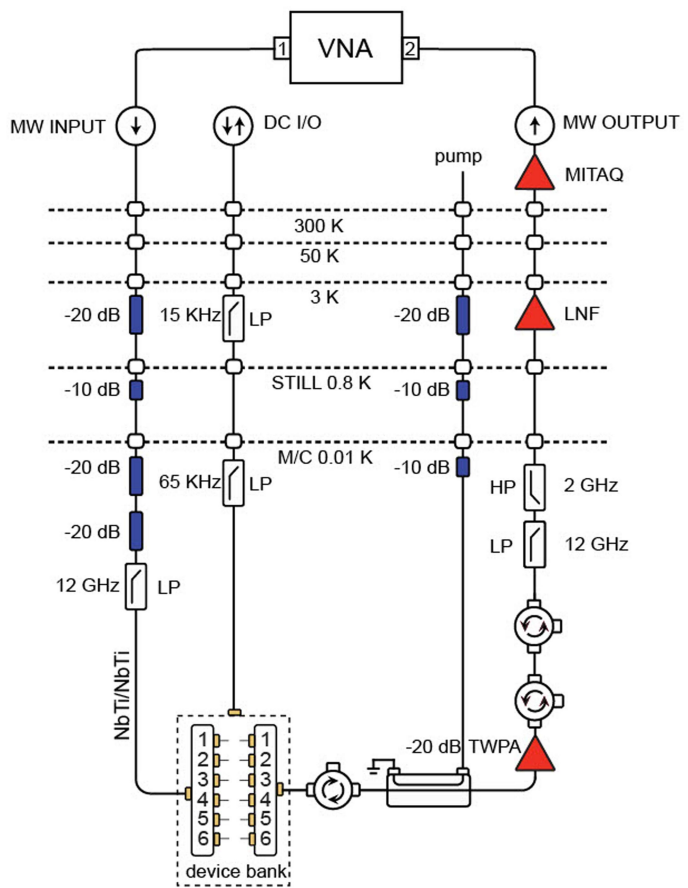
## Additional information

**Supplementary information** The online version contains supplementary material available at <https://doi.org/10.1038/s41586-024-08494-7>.

**Correspondence and requests for materials** should be addressed to Joel J.-W. Wang, Pablo Jarillo-Herrero or William D. Oliver.

**Peer review information** *Nature* thanks Fan Zhang and the other, anonymous, reviewer(s) for their contribution to the peer review of this work.

**Reprints and permissions information** is available at <http://www.nature.com/reprints>.

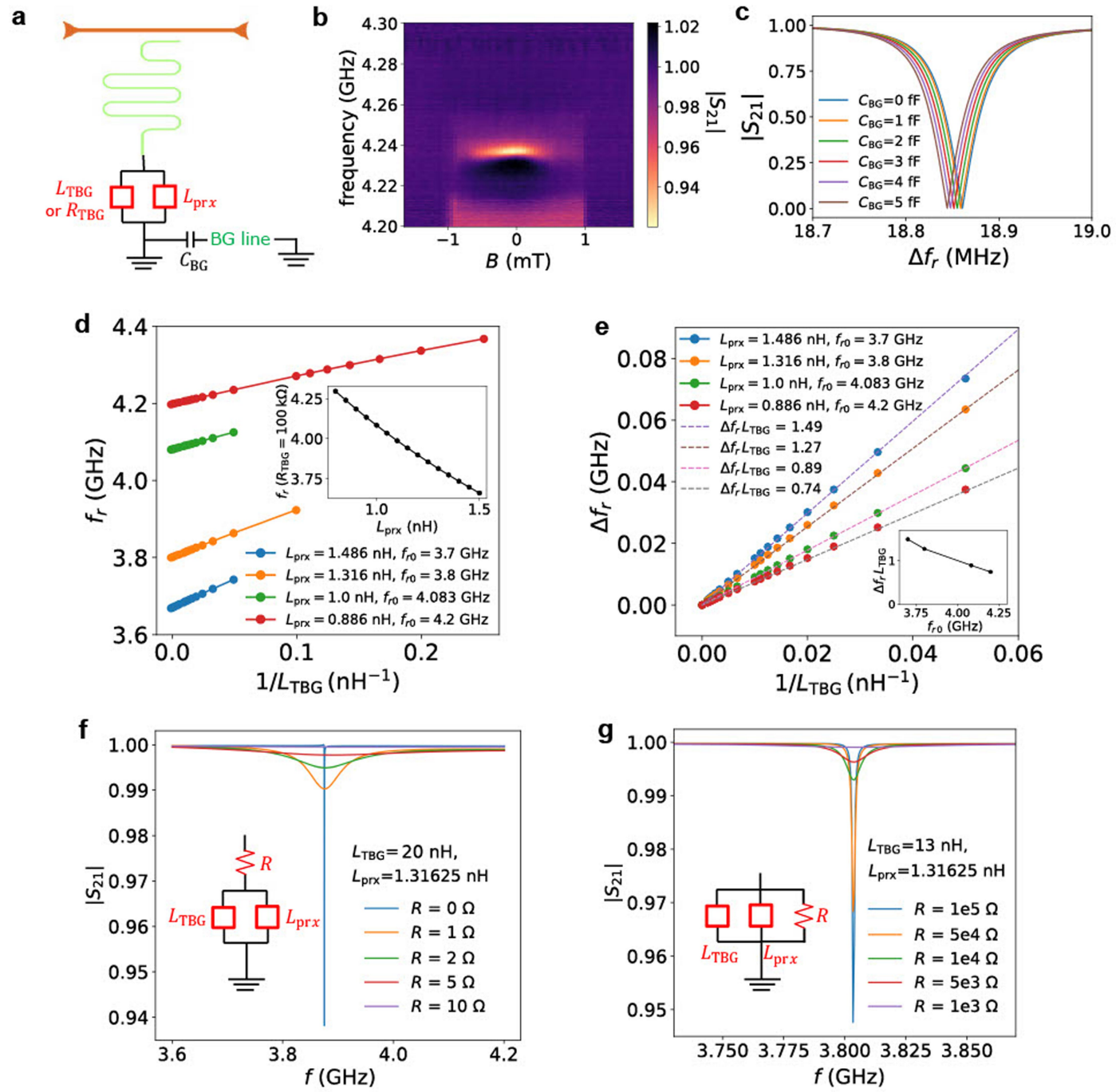


Key:

- █ = attenuator
- = circulator
- = feedthrough
- △ = amplifier

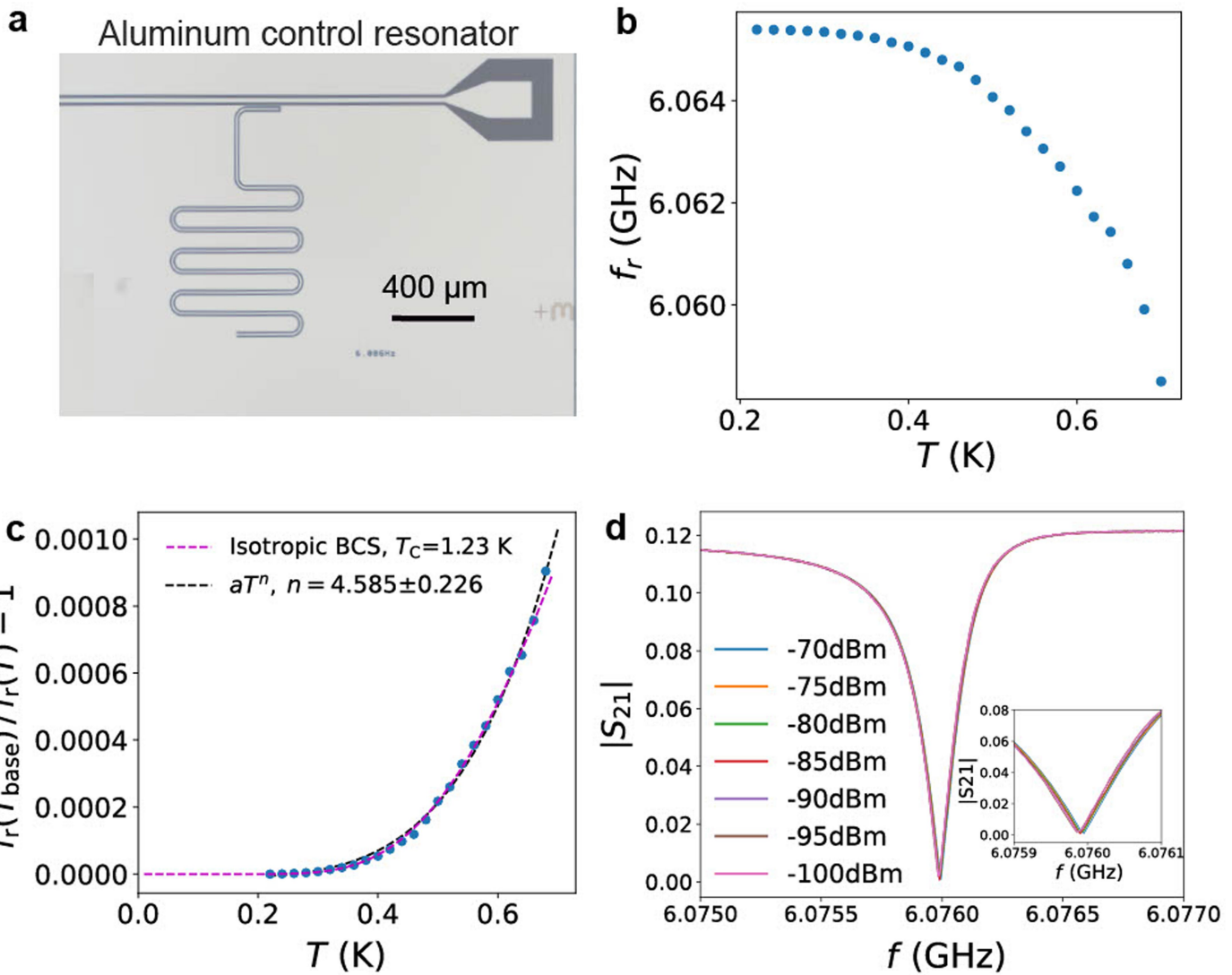
**Extended Data Fig. 1 | Microwave and DC characterization setup.** Wiring diagram in the dilution refrigerator, which includes attenuators, amplifiers, isolators, and filters.

# Article



**Extended Data Fig. 2 | Model and simulation of the resonator with termination.** **a**, Model used for the microwave simulation, including the through line, resonator, termination, and backgate. The termination includes both the MATBG (resistance or inductance, depending on bias point) and the proximitized edge inductance (independent of bias point). See main text. **b**, Out-of-plane magnetic field dependence of the resonance of Bernal-stacked bilayer graphene biased near its charge neutrality point. **c**, Simulated  $|S_{21}|$  as a function of  $\Delta f_r = f_r - 3.8$  GHz for different values of  $C_{\text{BG}}$  of the model. **d**, Simulated

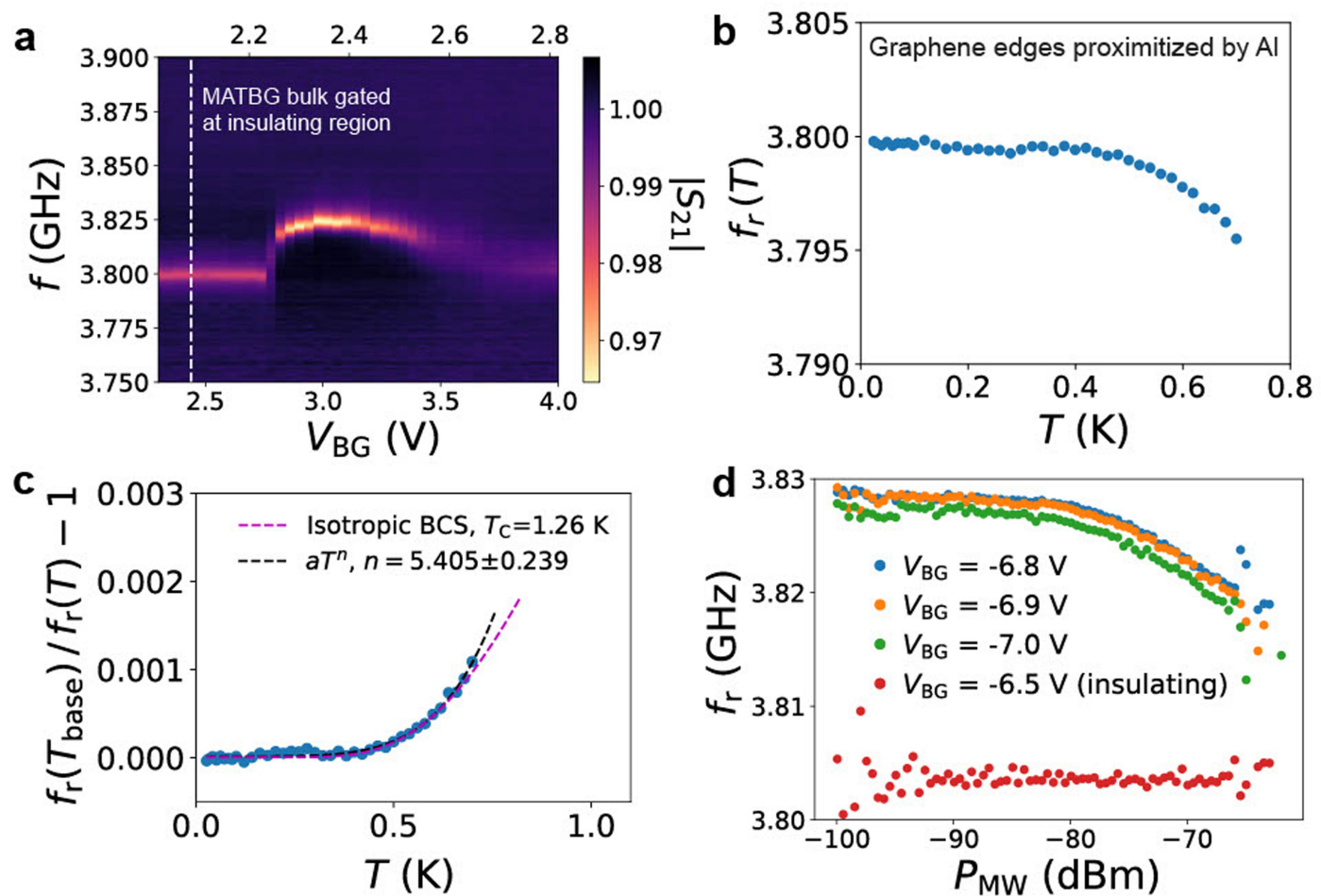
resonance frequency as a function of  $1/L_{\text{TBG}}$  for different values of  $L_{\text{prx}}$ .  $C_{\text{BG}}$  is fixed at 3 fF. **e**, Data in panel **d**, with the baseline resonance frequency subtracted. Dashed lines are the linear fit to the simulation data. Inset depicts the slope of the linear fit as a function of offset frequency  $f_{r0}$ , which depends on  $L_{\text{prx}}$ . **f,g**, Simulations of possible series (**f**) and parallel (**g**) contact resistances between the MATBG and the resonator, ground, and leads. Our results are most consistent with superconducting contacts, i.e., zero series resistance and large parallel resistance.



**Extended Data Fig. 3 | Temperature and power dependence of the resonant frequency for the aluminum-only  $\lambda/4$  resonator (control resonator).**

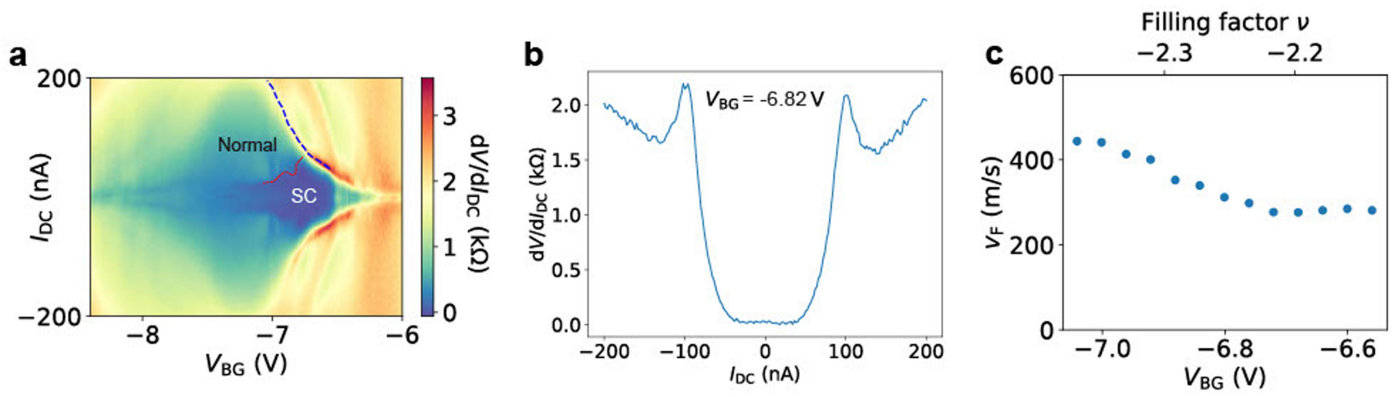
**a**, Microscope image of the aluminum-only  $\lambda/4$  resonator, terminated directly to ground with Al. **b**, Temperature dependence of the resonance for the aluminum-only  $\lambda/4$  resonator. **c**, Temperature dependence of  $f_r(T_{\text{base}})/f_r(T) - 1$

for the aluminum-only  $\lambda/4$  resonator as fit with the isotropic BCS model (exponential fit, purple dashed line) and a power-law fit (black dashed line). **d**,  $|S_{21}|$  for the aluminum-only  $\lambda/4$  resonator at  $T_{\text{base}} = 20 \text{ mK}$  for different microwave powers. The power independence indicates the negligible kinetic inductance for the thick (250 nm) aluminum resonator and termination.



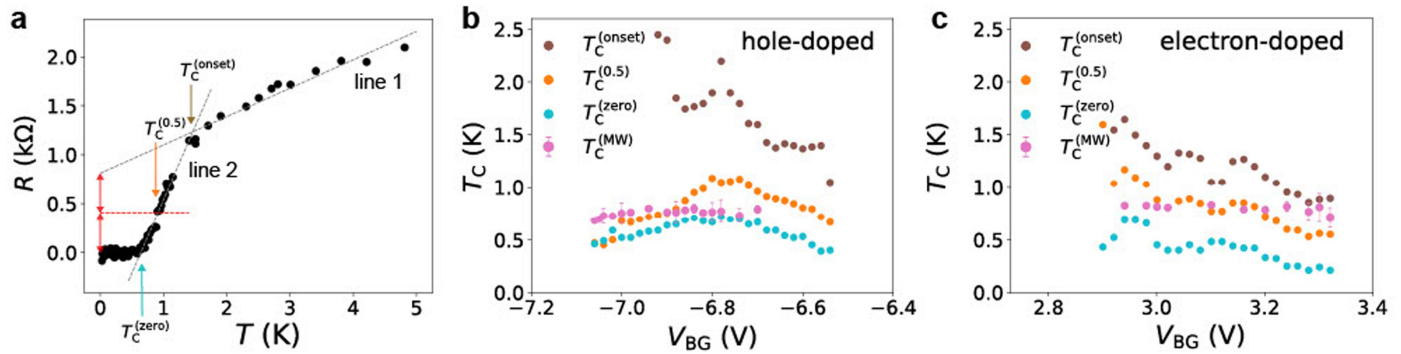
**Extended Data Fig. 4 | Temperature and power dependence of the resonant frequency for the resonator terminated by the Al-proximity-terminated graphene edge.** **a**, Gate dependence of the resonance in the MATBG-terminated resonator. The insulating region is indicated by a vertical white dashed line  $V_{BG} = 2.44$  V. The frequency at this point is used as the reference point when determining a frequency shift. **b**, Temperature dependence of the resonance for the MATBG-terminated resonator in the insulating region  $V_{BG} = 2.44$  V. **c**, Temperature dependence of  $f_r(T_{base})/f_r(T) - 1$  for the MATBG-terminated

resonator in the insulating region  $V_{BG} = 2.44$  V and fit with the isotropic BCS model (purple dashed line) and the power-law fit (black dashed line). The resonance no longer shifts below about 0.5 K. **d**, Microwave power dependence off  $f_r$  at  $V_{BG} = -6.8, -6.9, -7.0$  V (where the MATBG is superconducting) and  $V_{BG} = -6.5$  V (where the MATBG is insulating). In contrast to the MATBG traces, the proximitized edge does not vary substantially with power, indicating that its kinetic inductance is adopted from the aluminum leads and is relatively small compared with the bulk MATBG.



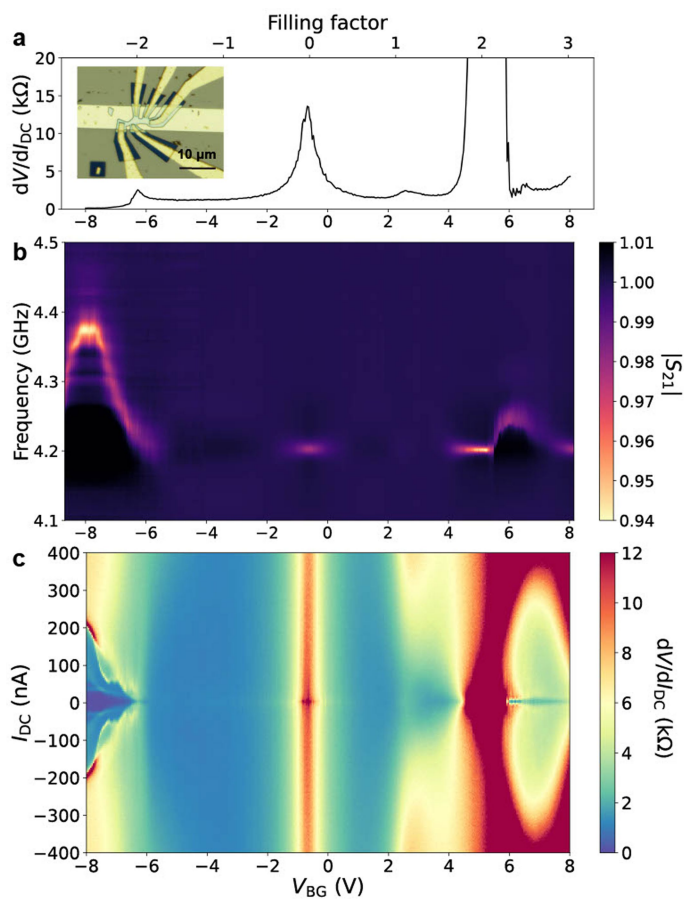
**Extended Data Fig. 5 | Estimation of Fermi velocity.** **a**, Differential resistance  $dV/dI_{DC}$  as a function of DC bias current  $I_{DC}$  and gate voltage  $V_{BG}$ . The blue dashed line indicates  $I_{cn}$ . **b**, Differential resistance  $dV/dI_{DC}$  as a function of DC bias current  $I_{DC}$  at  $V_{BG} = -6.82$  V. **c**, Gate dependence of the Fermi velocity, extracted from  $v_n = J_{cn}/\tilde{n} e$ .

# Article



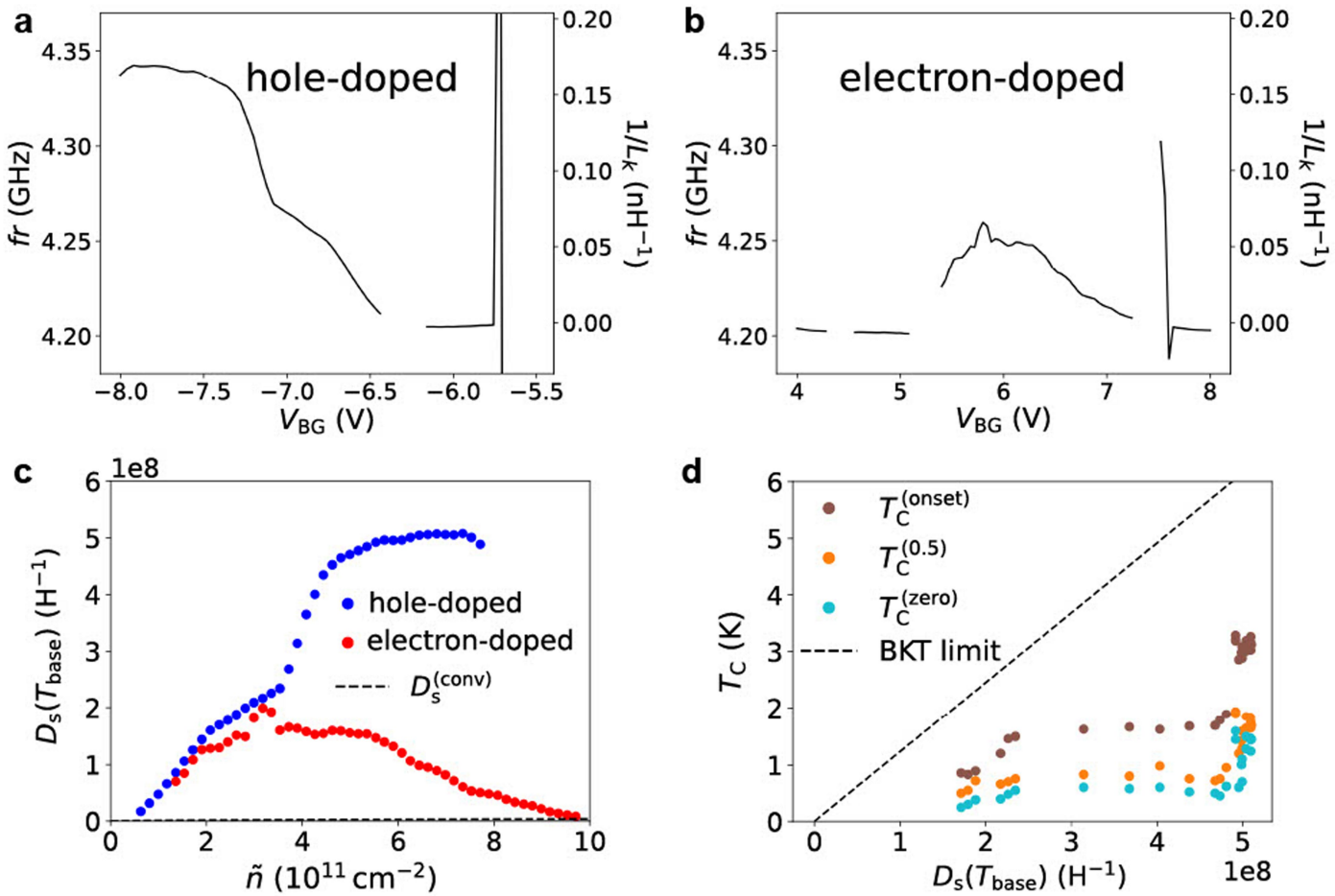
**Extended Data Fig. 6 | Determination of  $T_c$ .** **a**, The temperature dependence of the MATBG resistance at  $V_{BG} = -6.7$  V. Gray dashed lines represent linear fits. Red arrows and a red dashed line indicate the half value of line 1 at zero temperature. Critical temperatures are marked by arrows of different colors.

**b, c**, Backgate dependence of critical temperatures  $T_c^{(onset)}$ ,  $T_c^{(0.5)}$ , and  $T_c^{(zero)}$  as obtained from DC resistance measurements; and  $T_c^{(MW)}$  as obtained from microwave measurements in the hole-doped (**b**) and the electron-doped (**c**) regimes.



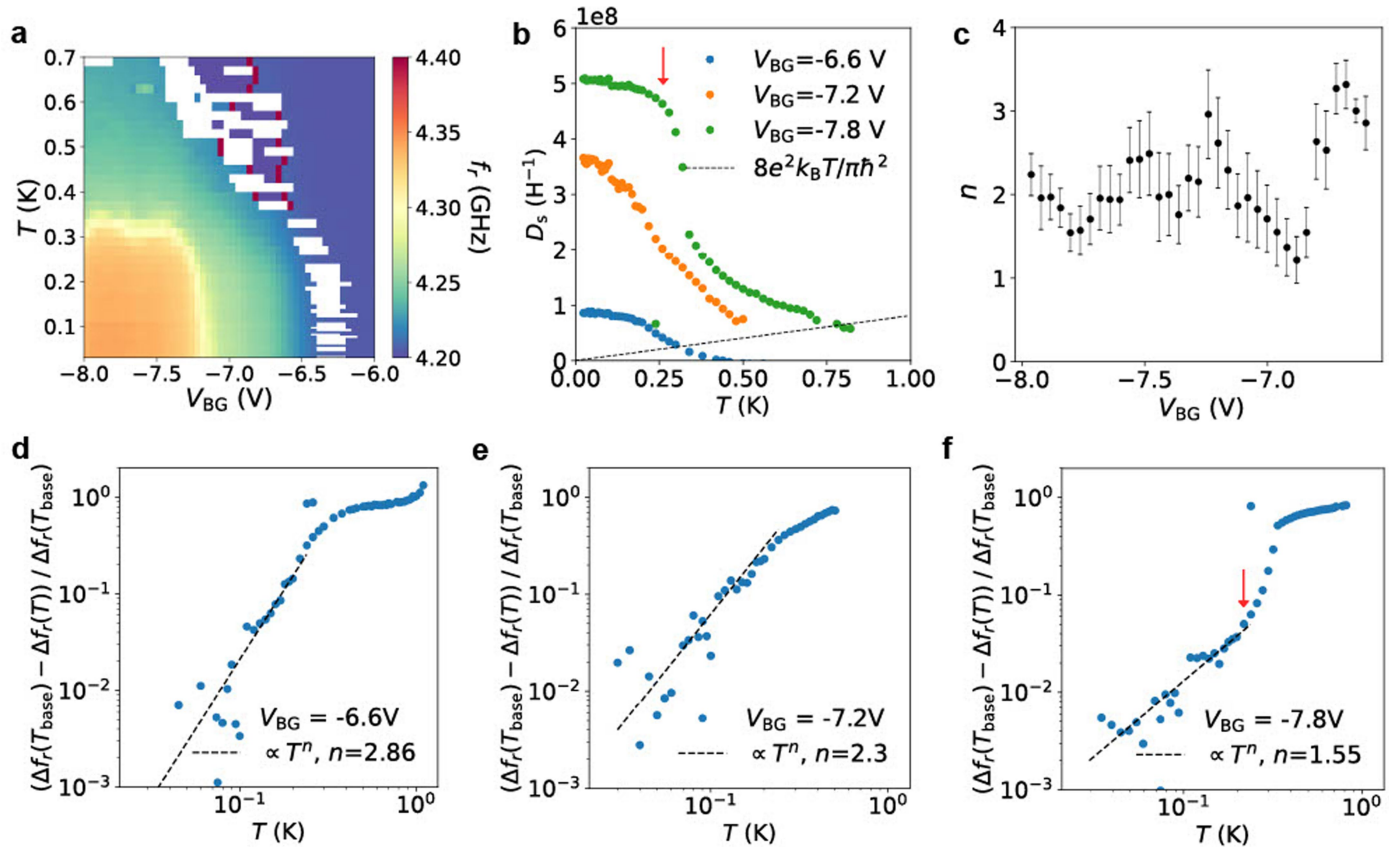
**Extended Data Fig. 7 | Gate dependence of DC and microwave response in the second device.** **a**, DC resistance  $R$  as a function of the backgate voltage  $V_{BG}$ . Top axis represents the filling factor  $v$ . Inset shows the optical microscope image of the second device. **b**, Microwave transmission coefficient  $|S_{21}|$  versus  $V_{BG}$ . The resonant frequency (bright line) shifts within the zero-resistance region in panel (a), near filling factors  $v = \pm 2$ . The resonance remains essentially constant within the high resistance region. **c**, Differential resistance  $dV/dI_{DC}$  as a function of  $V_{BG}$  and DC bias current  $I_{DC}$ .

## Article



**Extended Data Fig. 8 | Superfluid stiffness, carrier density, and critical temperature in the second device.** **a,b**, Frequency shift and inverse of the kinetic inductance as a function of  $V_{BG}$  in hole-doped (**a**) and electron-doped (**b**) regimes. **c**, Superfluid stiffness  $D_s$  at base temperature  $T_{base}$  as a function of effective carrier density  $\tilde{n}$ , measured with respect to  $|v| = 2$ . The black dashed

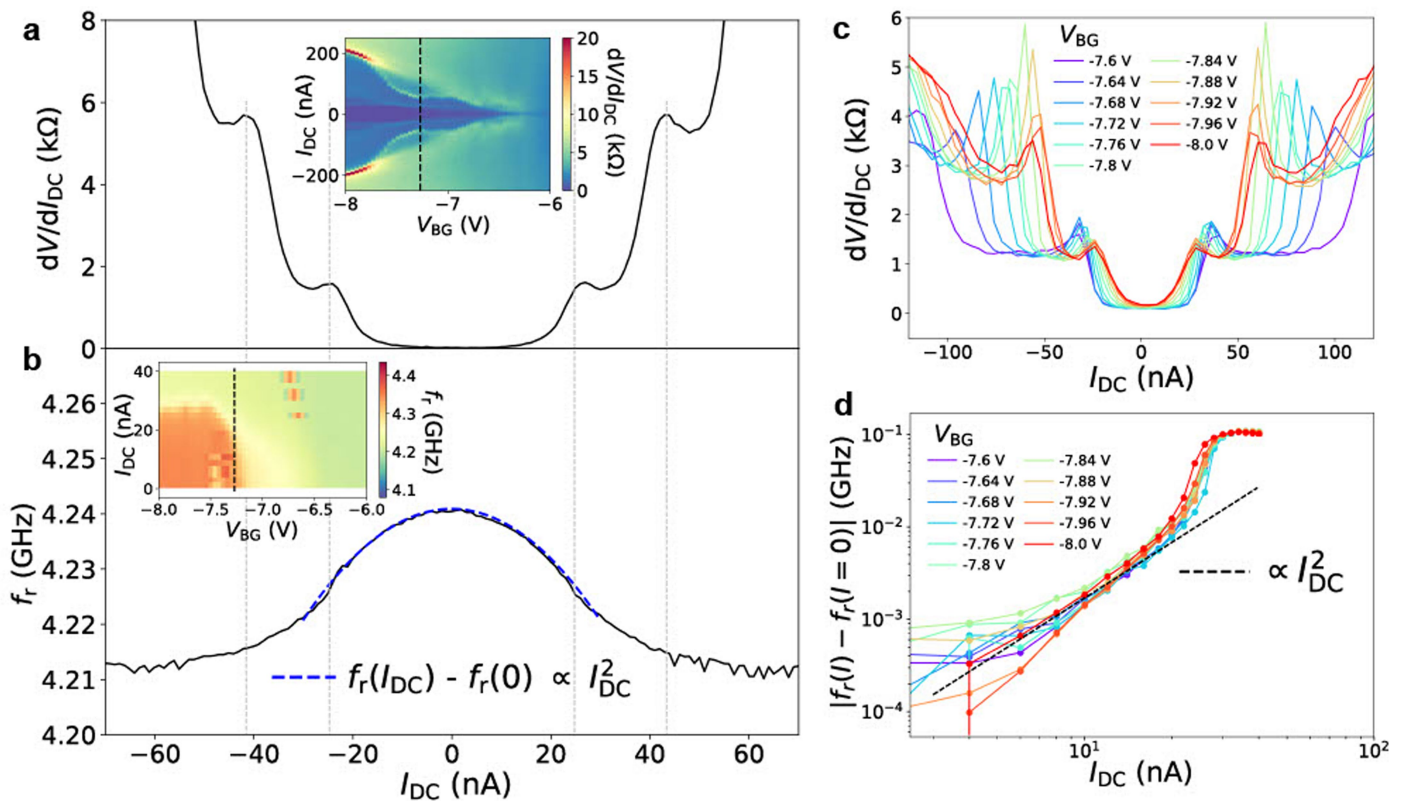
curve estimates the conventional contribution to the superfluid stiffness from single-band Fermi liquid theory:  $D_s^{(\text{conv})} = e^2 \tilde{n} v_F / \hbar k_F$ . **d**, Critical temperature  $T_c$  and corresponding superfluid stiffness  $D_s$  at base temperature  $T_{base}$  as tuned by  $V_{BG}$ . The black dashed line represents the BKT limit  $T_c = \pi \hbar^2 D_s(T_{base}) / 8e^2 k_B$ .



**Extended Data Fig. 9 | Temperature dependence in the second device.**

**a**, Resonance frequency  $f_r$  as a function of temperature and  $V_{BG}$ . **b**, Temperature dependence of the measured  $D_s$  at  $V_{BG} = -6.6$ ,  $-7.2$ , and  $-7.8$  V and  $8e^2 k_B T / \pi \hbar^2$  (black dashed line), where  $T_{BKT}$  is determined by their intersection. **c**,  $V_{BG}$

dependence of the exponent determined from the power-law fitting at  $T < 0.3 T_C$ . **d**, **e**, **f**, Power-law fitting of  $(\Delta f_r(T_{base}) - \Delta f_r(T)) / \Delta f_r(T_{base})$  at  $V_{BG} = -6.6$ ,  $-7.2$ , and  $-7.8$  V.



**Extended Data Fig. 10 | DC bias current dependence in the second device.**

**a**,  $I_{DC}$  dependence of the DC resistance  $dV/dI_{DC}$  at  $V_{BG} = -7.3$  V. Inset depicts the DC resistance as a function of  $I_{DC}$  and  $V_{BG}$ . **b**,  $I_{DC}$  dependence of  $f_r$  at  $V_{BG} = -7.3$  V. The blue dashed curve is the quadratic fit. Inset depicts  $f_r$  as a function of  $I_{DC}$  and  $V_{BG}$ .

and  $V_{BG}$ . **c**,  $I_{DC}$  dependence of the DC resistance over the hole-doped SC region.

**d**,  $I_{DC}$  dependence of  $|f_r(I) - f_r(0)|$  over the hole-doped SC region using a logarithmic scale. The black dashed line indicates the quadratic dependence.